

Fluidization dynamics of a simple yield stress fluid: a long way from transient shear banding to steady state

Thibaut Divoux,¹ David Tamarii,¹ Catherine Barentin,² and Sébastien Manneville^{1,3}

¹*Université de Lyon, Laboratoire de Physique, École Normale Supérieure de Lyon,
CNRS UMR 5672, 46 Allée d'Italie, 69364 Lyon cedex 07, France.*

²*Laboratoire de Physique de la Matière Condensée et Nanostructures,
Université de Lyon; Université Claude Bernard Lyon I,*

CNRS UMR 5586 - 43 Boulevard du 11 Novembre 1918, 69622 Villeurbanne cedex, France.

³*Institut Universitaire de France.*

(Dated: October 11, 2011)

The shear-induced fluidization of a carbopol microgel is investigated during long start-up experiments using combined rheology and velocimetry in Couette cells of varying gap widths and boundary conditions. As already described in [Divoux et al., *Phys. Rev. Lett.*, 2010, **104**, 208301], we show that the fluidization process of this simple yield stress fluid involves a transient shear-banding regime whose duration τ_f decreases as a power law of the applied shear rate $\dot{\gamma}$. We complete our previous findings by an investigation of the influence of the shearing geometry through the gap width e and the boundary conditions. While slip conditions at the walls seem to have a negligible influence on the fluidization time τ_f , different fluidization processes are observed depending on $\dot{\gamma}$ and e : the shear band remains almost stationary for several hours at low shear rates or small gap widths before strong fluctuations lead to a homogeneous flow whereas at larger values of $\dot{\gamma}$ or e , the transient shear band is seen to invade the whole gap in a much smoother way. Finally, by comparing local and global rheological measurements, we emphasize that the steady state reached by our samples is fully compatible with that expected for a simple yield stress fluid described by a Herschel-Bulkley behaviour.

PACS numbers:

I. INTRODUCTION

A huge amount of soft materials display solid properties at rest and under relatively small shear stresses while they become fluid above a typical stress known as the “yield stress” [1]. Examples range from daily products such as the foams or emulsions encountered in foods and cosmetics to drilling muds and granular materials [2]. This property is also shared by both hard and soft jammed colloids [3]. Besides intense debate over the right experimental procedure to measure the yield stress [4], –or even on its very existence [5, 6]–, the question of how a yield stress material turns from solid to liquid under shear remains largely unexplored. In fact, previous works have mainly focused on the steady state reached by the material after yielding, with emphasis on whether or not the stationary flow field displays shear banding, i.e. whether an unsheared solid region coexists with a fluidized region characterized by a finite local shear rate at steady state or whether the whole sample flows homogeneously with a finite shear rate [7, 8]. This has led to distinguish between “simple” yield stress fluids (which do not show steady-state shear banding) and “thixotropic” yield stress fluids (which display solid–fluid coexistence at steady-state) [9, 10]. It is acknowledged that simple yield stress fluids encompass foams, emulsions, and some microgels such as the carbopol dispersions considered in the present work, and that their steady-state rheology follows a Herschel-Bulkley behaviour [5, 11, 12]: $\sigma = \sigma_c + \tilde{\eta}\dot{\gamma}^n$, where σ is the shear stress, σ_c is the yield stress, $\dot{\gamma}$ is

the shear rate, and $\tilde{\eta}$ and $n = 0.2\text{--}1$ are phenomenological parameters. On the other hand, colloidal gels and clay suspensions are generally thixotropic not only in the sense of steady-state shear banding [13] but also in the common rheological sense [14]. However, in spite of this apparently simple distinction, clearly differentiating the two kinds of yield stress fluids may turn out to be experimentally quite difficult, first because of vanishingly small flow velocities and shear rates close to yielding and second because of transient regimes that can become critically long. To overcome these difficulties spatially and temporally resolved measurements are required on time scales long enough to ensure that a steady state has been reached.

In order to assess the slow yielding dynamics of a simple yield stress fluid, we have recently used ultrasonic velocimetry coupled to standard rheology in carbopol samples sheared in a small-gap concentric cylinder cell (Couette cell) [15]. We have shown that, under a given imposed shear rate, the transition from solidlike to fluidlike behaviour involves a transient regime characterized by shear banding: a fluidized band is generated at the inner rotating cylinder and, after a time τ_f called the “fluidization time” that can reach 10^5 s, it invades the whole gap of the Couette cell. τ_f was shown to follow a power-law dependence on the imposed shear rate: $\tau_f \sim \dot{\gamma}^{-\alpha}$ with $\alpha = 2\text{--}3$, independent of the shearing geometry but depending on the protocol for sample preparation and on the carbopol concentration. At short times, the shear band grows from a thin lubrication layer that is generated at the inner wall as the sample suddenly fails after

a period of elastic loading, for both rough and smooth boundary conditions. This short-time behaviour, which has been described in detail elsewhere [16], is fully correlated with the presence of a stress overshoot in the rheological response of the material.

Finally, experiments under controlled shear stress [17] have shown that a similar fluidization scenario is at play during creep tests above the yield stress and that the fluidization time follows a power law of the viscous stress $\sigma - \sigma_c$: $\tau_f \sim (\sigma - \sigma_c)^{-\beta}$ with $\beta = 4-6$. By comparing the power laws obtained under imposed shear rate and shear stress, one recovers the Herschel-Bulkley behaviour, in which the exponent n naturally appears as the ratio of the two fluidization exponents $n = \alpha/\beta$. This leads to an original point of view linking the steady-state rheology of the material to transient fluidization processes characterized by critical-like behaviours.

The present article is meant to complete our previous work under controlled shear rate [15]. We provide a full investigation of the transient shear banding phenomenon during start-up experiments at a given applied shear rate, based on data sets recorded in smooth Couette cells. The paper is structured as follows. Section II describes the materials and methods used to investigate yielding of carbopol dispersions. Our results are gathered in Sect. III. We first give a qualitative description of the transient shear banding phenomenon. The applied shear rate is then varied to evidence the power law followed by the fluidization time τ_f . We also focus on the influence of the shearing geometry on the fluidization dynamics by varying the gap width. Finally, Sect. IV further discusses the possible effects of boundary conditions and provides a link between steady-state local and global rheology.

II. EXPERIMENTAL

A. Preparation of carbopol samples

We focus on aqueous dispersions of carbopol ETD 2050 at a concentration of 1 % w/w. Carbopol powder contains homo- and copolymers of acrylic acid highly cross-linked with a polyalkenyl polyether [5, 18]. Once the polymer is dispersed into water, adequate pH conditions lead to polymer swelling. Swollen polymer particles get jammed into an amorphous assembly referred to as a “microgel.” The typical size of the soft particles range from a few microns to roughly 20 microns [19–21]. The exact microstructure depends on the type of carbopol, [18] on its concentration, [5] and on the details of the preparation protocol [18, 20, 22]. Carbopol microgels are known to be non-aging, non-thixotropic simple yield stress fluids [6, 23–25] and their steady-state flow curve nicely follows the Herschel-Bulkley law:

$$\sigma = \sigma_c + \tilde{\eta} \dot{\gamma}^n, \quad (1)$$

with $n = 0.3-0.6$ depending on the type of carbopol and its concentration [5, 15, 21, 24].

Our preparation protocol has been described in detail elsewhere [16, 17]. As already noted, due to variations of the final pH ($6.5 < \text{pH} < 7.5$), the properties of our samples may vary from batch to batch. Therefore, if one wants to compare quantitatively results obtained in various geometries, gaps, or boundary conditions, one should ensure that batches with the same final pH are used. This issue will be mentioned whenever relevant for the present experiments.

It is also important to recall that, in order to perform ultrasonic velocimetry measurements, our samples are seeded with micron-sized hollow glass spheres at 0.5 % w/w (Potters, Sphericel, mean diameter 6 μm , density 1.1) to provide acoustic contrast to the samples [26]. We have shown previously that the addition of these glass spheres has little influence on the sample rheological properties: [16] it only stiffens the material by about 10 %. The fact that seeding has no impact on the rheological response of our carbopol microgel during yielding will be further demonstrated in the present study. To this aim, we also prepare 1 % w/w “pure” carbopol microgels, i.e. samples that are free of acoustic contrast agents.

B. Rheological measurements

Rheological measurements are performed using stress-controlled rheometers (Anton Paar MCR 301 and TA Instruments AR1000N). Here, we shall mainly focus on experiments performed in a polished Plexiglas Couette geometry with a height of 28 mm, a rotating inner cylinder of radius 24 mm, and a fixed outer cylinder of radius 25 mm, yielding a gap width $e = 1$ mm. The surface roughness of polished Plexiglas is about 15 nm as measured from atomic force microscopy, which will be referred to as “smooth” in the following. Other polished Plexiglas rotors of radii 24.55, 23.5 and 22 mm will be used to vary the gap width, yielding respectively $e = 0.45, 1.5$, and 3 mm.

Besides these smooth Couette cells, we will briefly discuss results obtained in a rough Couette cell (height 28 mm, rotating inner cylinder radius 23.5 mm, fixed outer cylinder radius 24.6 mm, gap width $e = 1.1$ mm) where sandpaper was glued on both shearing surfaces to provide a roughness of 60 μm . Mixed boundary conditions will also be tested in a Couette cell of height 28 mm and gap width 1.6 mm where only the rotating cylinder was covered with sandpaper of roughness 60 μm while the fixed outer cylinder is the same as for smooth Couette cells. Finally, a rough plate-and-plate geometry (radius 21 mm, gap width $e = 1$ mm, roughness 162 μm) as well as a smooth aluminum cone-and-plate geometry (radius 25 mm, cone angle 2°) will be used to check for the rheological signature of transient shear banding in complementary geometries.

Before starting an experiment, preshear is applied for 1 min at $+1000 \text{ s}^{-1}$ and for 1 min at -1000 s^{-1} to erase

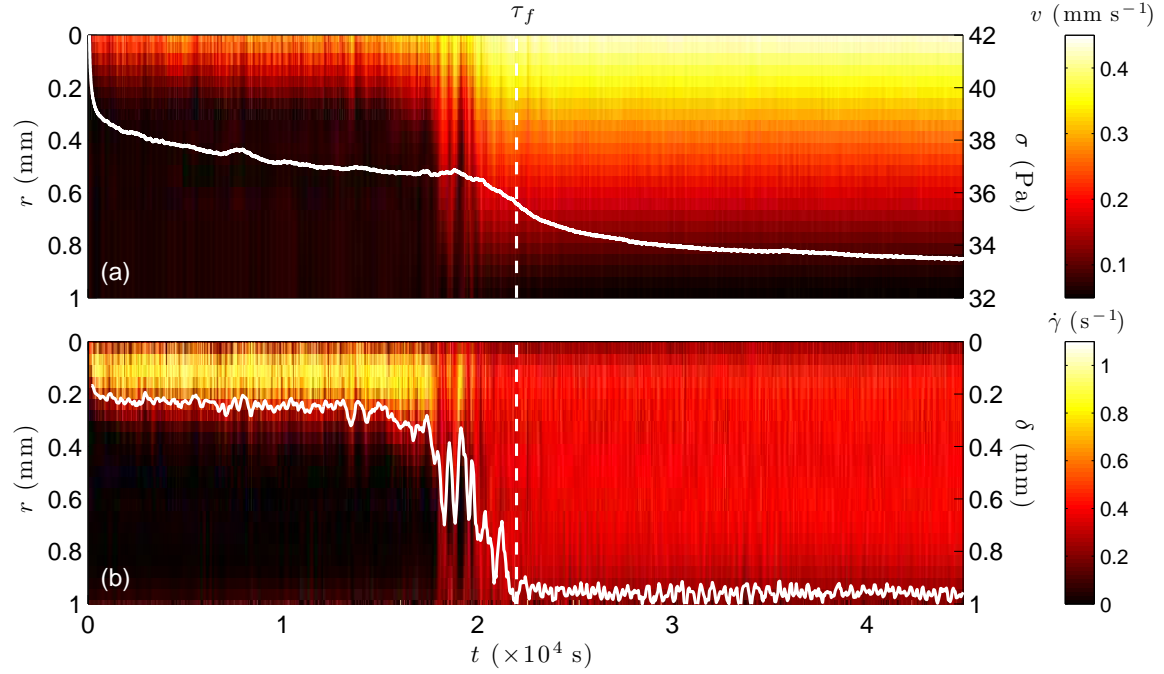


FIG. 1: (a) Spatiotemporal diagram of the velocity data $v(r, t)$ as a function of position r and time t . A constant shear rate $\dot{\gamma} = 0.5 \text{ s}^{-1}$ is applied at time $t = 0$ to a 1 % w/w carbopol microgel seeded with 0.5 % w/w hollow glass spheres in a smooth Couette cell of gap width 1 mm. The radial position r (left vertical axis) is measured from the rotating inner wall. Also shown with a white line is the stress response $\sigma(t)$ (right vertical axis). (b) Spatiotemporal diagram of the local shear rate $\dot{\gamma}(r, t)$. The white line shows to the position $\delta(t)$ of the interface between the fluidized band and the solidlike region. The vertical dashed line indicates the fluidization time τ_f , i.e. the time at which the shear rate field becomes homogeneous.

the loading history. The viscoelastic moduli are then monitored for 2 min. We found that both the elastic and the viscous moduli no longer vary significantly after 2 min. Finally, the sample is left at rest for 1 min to ensure that a reproducible initial state is reached. The reader is referred to Ref. [16] for more details about the rheological protocol and the viscoelastic properties of our samples at rest.

C. Ultrasonic velocimetry

In the Couette geometry, velocity profiles across the gap can be recorded with a spatial resolution of 40 μm using ultrasonic speckle velocimetry (USV). Full technical details about USV can be found in Ref. [26]. Here, the sample velocity field is measured at about 15 mm from the cell bottom simultaneously to the global rheological response. This allows for a direct correlation between time-resolved velocimetry and rheological data. The temporal resolution depends on the imposed shear rate and varies from about 50 s per velocity profile at the lowest shear rates ($\dot{\gamma} \lesssim 0.5 \text{ s}^{-1}$) to less than 1 s for $\dot{\gamma} \gtrsim 10 \text{ s}^{-1}$.

III. RESULTS

A. General description of the fluidization process

In this section, we describe qualitatively the fluidization process recorded after a shear rate $\dot{\gamma} = 0.5 \text{ s}^{-1}$ is applied at time $t = 0$ to a carbopol sample in the smooth Couette cell. Figure 1(a) shows the spatiotemporal diagram where the velocity data $v(r, t)$ is coded in colour levels. Time t and the radial position r measured from the inner wall respectively correspond to the horizontal and to the vertical axis. The white line in Fig. 1(a) corresponds to the stress response $\sigma(t)$ recorded by the rheometer simultaneously to the local velocity and will be discussed in the next section.

The spatiotemporal diagram of Fig. 1(b) shows the local shear rate $\dot{\gamma}(r, t)$ derived from the previous velocity data: $\dot{\gamma}(r, t) = r \partial(v(r, t)/r) \partial r$ where a second order differentiation scheme was used. To further reduce the noise level in the spatial derivative, $\dot{\gamma}(r, t)$ was smoothed using a moving average over four neighbouring points along the r -axis. From the spatiotemporal representation of $\dot{\gamma}(r, t)$, it is clear that the flow is spatially heterogeneous for $t \lesssim 2.10^4$ s: a strongly sheared region close to the rotor ($r < 0.3 \text{ mm}$) coexists with a solidlike region where the local shear rate vanishes ($r > 0.3 \text{ mm}$). This heterogeneous flow remains almost stationary for about 5 hours.

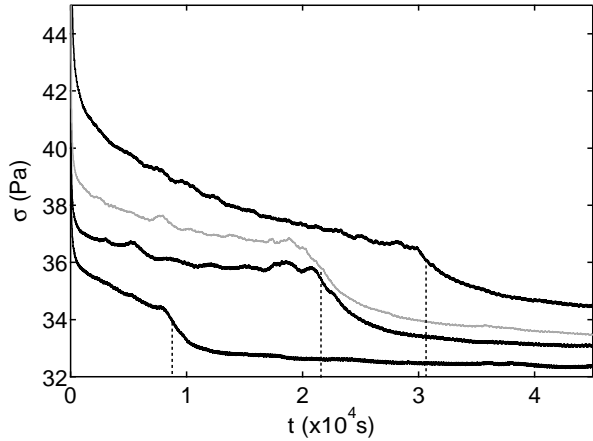


FIG. 2: Shear stress σ as a function of time t in a 1 % w/w “pure” carbopol microgel for different applied shear rates $\dot{\gamma} = 0.35, 0.5$, and 0.7 s^{-1} (black lines, from top to bottom). The grey line is the stress response of the seeded microgel for $\dot{\gamma} = 0.5 \text{ s}^{-1}$ already shown in Fig. 1(a). Experiments performed in a smooth Couette cell of gap width 1 mm. The vertical dashed lines indicate the fluidization times as derived from the inflection points of $\sigma(t)$.

At $t \sim 2.10^4 \text{ s}$, the flow undergoes dramatic changes: strong fluctuations occur that lead to a completely homogeneous flow at larger times.

Therefore, although the microgel fluidization process starts with a long-lasting shear-banding regime, this heterogeneous flow does *not* correspond to the steady state which is rather characterized by the homogeneous shear rate field indeed expected for simple yield stress fluids. This fluidization scenario is entirely similar to that already described for a rough geometry [15], which highlights its robustness with respect to boundary conditions.

B. Rheological signature of transient shear banding

As seen from the stress response $\sigma(t)$, superimposed to USV data as a white line in Fig. 1(a), global rheological measurements strongly reflect the transient behaviour observed in simultaneous yet independent local velocity measurements. For $t \lesssim 2.10^4 \text{ s}$, the shear stress slowly decays with noticeable fluctuations. Around $t \sim 2.10^4 \text{ s}$, $\sigma(t)$ starts decreasing much more steeply before slowly leveling off to its steady-state value. Remarkably, the inflection point in the stress relaxation nicely corresponds to the time τ_f at which the flow becomes homogeneously sheared (see vertical dashed lines in Fig. 1). The presence of such a strong rheological signature indicates that the fluidization process, observed with USV at about 15 mm from the cell bottom, probably occurs on a similar timescale throughout the whole height of the Couette cell.

Note that the sharp decrease of the stress at the shortest times is due to the presence of a stress overshoot that

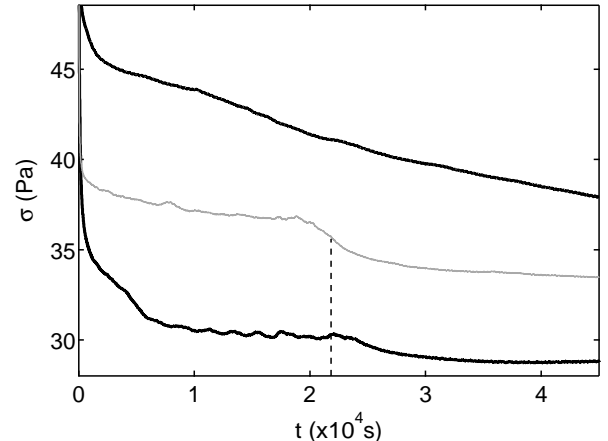


FIG. 3: Shear stress σ as a function of time t in two different geometries for similar shear rates: a rough plate-and-plate geometry (top black curve, $\dot{\gamma} = 0.4 \text{ s}^{-1}$) and a smooth cone-and-plate geometry (bottom black curve, $\dot{\gamma} = 0.5 \text{ s}^{-1}$). Experiments performed on the same batch of 1 % w/w carbopol microgels seeded with hollow glass spheres. This batch is different from that used previously in Fig. 1. The grey line is the stress response for $\dot{\gamma} = 0.5 \text{ s}^{-1}$ in a smooth Couette geometry of gap width 1 mm already shown in Fig. 1(a)

occurs for a strain $\gamma = \dot{\gamma}t \simeq 1$ but does not clearly show here due to the choice of vertical and horizontal scales. The stress overshoot phenomenon in the same carbopol microgels has been thoroughly investigated in Ref. [16]. In particular, by focusing on the initial stage of the material response, we have shown that the stress first grows linearly with time. This is indicative of an elastic loading of the material, which is confirmed by the homogeneous strain field measured using USV. The stress overshoot then corresponds to a proliferation of plastic events that leads to the failure of the sample at the inner wall. This sudden failure gives way to total wall slip at the rotor. The shear band observed here then nucleates from the lubrication layer at the rotor. Full details about the stress overshoot and its correlation to the local flow behaviour can be found in Ref. [16].

Moreover, it is important to mention that, as seen in Fig. 2 for various applied shear rates, the above rheological signature of transient shear banding is also observed in a “pure” carbopol sample, i.e. one that is free of seeding glass spheres. For $\dot{\gamma} = 0.5 \text{ s}^{-1}$, the stress response is even quantitatively very close to that recorded at the same shear rate in the sample seeded with 0.5 % w/w hollow glass spheres (grey line in Fig. 2). Although no local velocimetry is available for the “pure” sample, the very similar rheological response is surely indicative of the same fluidization process. We infer from Fig. 2 that our contrast agents have no significant influence on the transient shear banding phenomenon.

We also check in Fig. 3 that such a striking feature is also seen in the cone-and-plate geometry. In that case, the “kink” in $\sigma(t)$ for $\dot{\gamma} = 0.5 \text{ s}^{-1}$ again coincides with

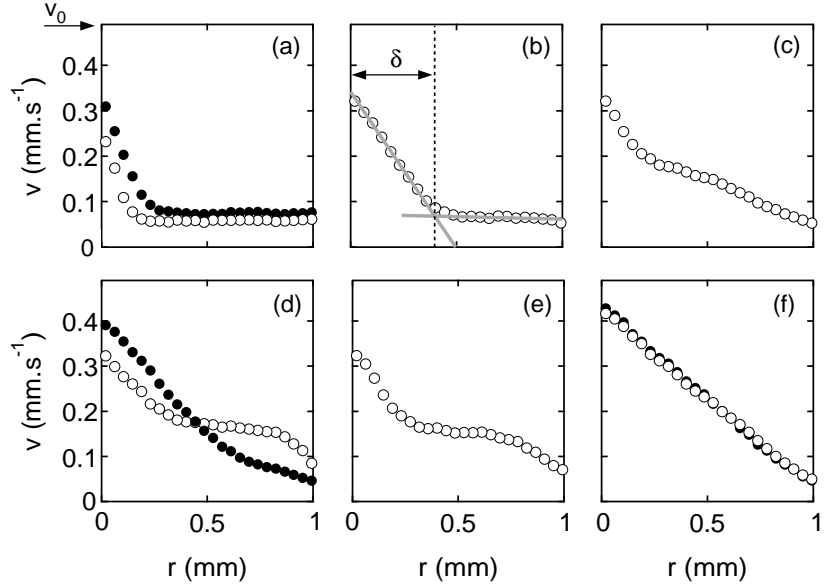


FIG. 4: Velocity profiles $v(r, t)$ extracted from the data shown in Fig. 1 for (a) $t = 251$ s (\circ) and $t = 7563$ s (\bullet), (b) $t = 16720$ s, (c) $t = 18021$ s, (d) $t = 18671$ s (\circ) and $t = 18871$ s (\bullet), (e) 19422 s, and (f) $t = 30981$ s (\circ) and $t = 42742$ s (\bullet). The fitting procedure used to extract the slip velocities, the local shear rates in the two shear bands, and the position of the interface between the shear bands is illustrated by the grey lines in (b) (see text). Experiment performed in a smooth Couette cell of gap width 1 mm under an applied shear rate $\dot{\gamma} = 0.5 \text{ s}^{-1}$.

that observed in the Couette geometry, in spite of a shift in the absolute value of the stress which may be attributed to the fact that these experiments were performed on different microgel batches. However, in the plate-and-plate, a kink followed by an inflection point is far more difficult to detect: in this case, the fluidization time could be virtually anywhere above 10^4 s. This is most probably due to the large shear rate heterogeneity in the plate-and-plate geometry, where the local shear rate varies from zero at the rotation axis to the applied value $\dot{\gamma}$ at the plate periphery. We shall see in Sect. III D that the fluidization time increases dramatically with decreasing shear rates. Therefore, the fluidization process in a plate-and-plate geometry could be seen as the superposition of fluidization processes with widely different timescales, leading to a stress response that does not show very sharp features. Finally, it is worth noticing that the surface roughness of the shearing tools does not seem to play any prominent role since the exact same shape has also been reported for $\sigma(t)$ in a Couette cell of surface roughness $60 \mu\text{m}$ [15].

To conclude, the transient shear banding phenomenon and the subsequent fluidization have a characteristic rheological signature that appears very robust with respect to the shearing geometry and to the boundary conditions, at least for the low shear rates reported so far ($\dot{\gamma} = 0.3$ – 0.7 s^{-1}). In the following, we shall show that the kink in the stress response actually disappears when the shear rate or the gap width is increased, although transient shear banding is still observed through USV.

C. Quantitative analysis of the velocity profiles

Velocity profiles typical of the various stages of the fluidization process were extracted from the data in Fig. 1(a) and plotted in Fig. 4: quasi-stationary shear-banded velocity profiles for $t < 1.7 \cdot 10^4$ s [Fig. 4(a) and (b)], strongly fluctuating profiles for $t \sim 1.7$ – $2 \cdot 10^4$ s [Fig. 4(c–e)], and fully fluidized, homogeneous and stationary profiles for $t > 2 \cdot 10^4$ s [Fig. 4(f)]. A movie of the velocity profiles is also available as supplementary material.[†] During the abrupt fluidization at $t \sim 2 \cdot 10^4$ s, velocity profiles with three bands are observed transiently as in Fig. 4(d) and (e). Such strong fluctuations and anomalous velocity profiles are reminiscent of those observed in laponite suspensions sheared in a smooth geometry [27, 28]. Here however, no periodic oscillations between banded and linear velocity profiles are observed and these erratic fluctuations are observed over a rather limited time period compared to the total duration of the transient regime.

Important quantitative information can be readily extracted from individual velocity profiles. As shown in Fig. 4(b), linear fits in both shear bands directly yield the local shear rates $\dot{\gamma}_{\text{loc}}$ in the flowing and solidlike regions respectively. Extrapolating these fits to $r = 0$ and $r = e$ allows one to estimate the microgel velocities $v(r = 0)$ and $v(r = e)$ at the vicinity of the shearing surfaces, and therefore the slip velocities v_s at both walls, as well as the effective shear rate $\dot{\gamma}_{\text{eff}} = [v(r = 0) - v(r = e)]/e$. Finally, the intersection of the two linear fits yields the position δ of the interface between the fluidized and solid-

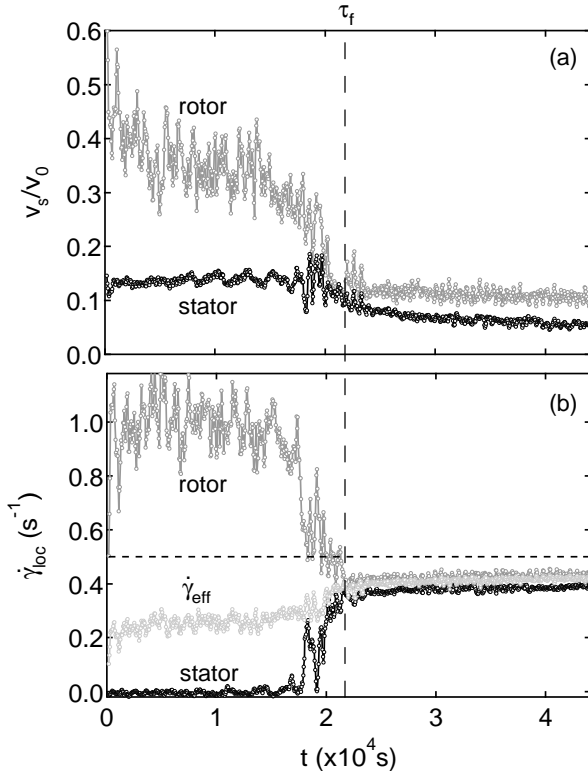


FIG. 5: Analysis of the velocity data shown in Fig. 1. (a) Slip velocities v_s at the stator (black) and at the rotor (grey). (b) Local shear rates $\dot{\gamma}_{loc}$ at the stator (black) and at the rotor (grey) together with the effective shear rate $\dot{\gamma}_{eff}$ (light grey). The vertical dashed line indicates the fluidization time τ_f . The horizontal dotted line in (b) shows the shear rate applied by the rheometer $\dot{\gamma} = 0.5$ s $^{-1}$. Experiment performed in a smooth Couette cell of gap width 1 mm.

like regions. In the data presented in Fig. 5, an additional moving average over four consecutive data points in time is applied to $v_s(t)$, $\dot{\gamma}_{loc}(t)$, $\dot{\gamma}_{eff}(t)$, and $\delta(t)$ in order to smooth out noise on short timescales.

It can be checked that our determination of δ , plotted both in Fig. 1(b) as a white line and in Fig. 6 as a grey line, indeed corresponds to the transition from high local shear rate to zero shear in the transient shear-banding regime. The fluidization time τ_f is then defined as the time at which the shear band totally disappears, i.e. $\delta(\tau_f) \simeq e$. The fact that δ never reaches exactly e is due to our procedure based on the intersection of two fits that use at least two data points close to the walls. Still, τ_f is always a well-defined quantity as shown by the dashed line in Fig. 1(b).

Figure 5 shows the results of the analysis of the velocity data of Fig. 1(a). An important amount of wall slip is observed throughout the shear banding regime with slip velocities up to 40 % of the rotor imposed velocity v_0 at the rotating inner wall and up to 15 % of v_0 at the fixed outer wall [see Fig. 5(a)]. Both slip velocities drop by about a factor of two as the shear band disappears and the flow becomes homogeneous around τ_f . In

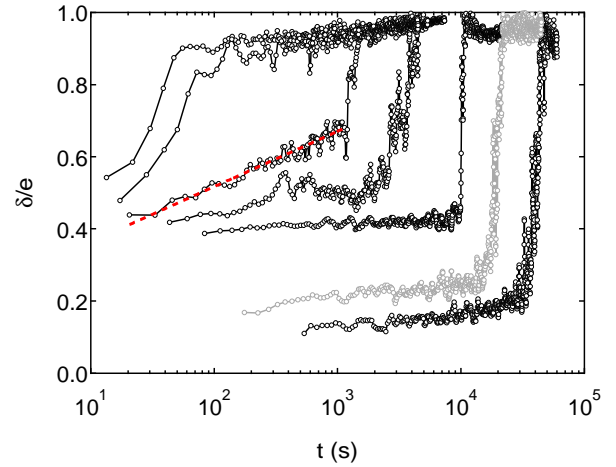


FIG. 6: Width δ of the shear band normalized by the gap width e versus time for different applied shear rates $\dot{\gamma} = 0.35$, 0.5 , 0.9 , 1.5 , 2.0 , 2.3 , and 3.0 s $^{-1}$ from right to left. The fluidization time strongly decreases with $\dot{\gamma}$. The gray line corresponds to the shear rate $\dot{\gamma} = 0.5$ s $^{-1}$ shown in Fig. 1. The red dashed line is a logarithmic fit for $\dot{\gamma} = 2.0$ s $^{-1}$ and $t < 10^3$ s. Experiments performed in a smooth Couette cell of gap width 1 mm.

steady state, the slip velocities relative to v_0 are about 10 % at the rotor and 5 % at the stator. This should be contrasted to our previous results in a rough Couette cell where the steady state did not show any significant wall slip [15].

The above evolution of the slip velocities is reflected in the effective shear rate: $\dot{\gamma}_{eff}$ first increases very slowly from about 0.2 to 0.3 s $^{-1}$ in the shear-banding regime and then more rapidly up to roughly 0.4 s $^{-1}$, which remains significantly below the imposed value of 0.5 s $^{-1}$ due to the presence of wall slip in steady state [see Fig. 5(b)]. As expected from the velocity profiles, the local shear rate close to the stator remains zero until the flow field shows strong fluctuations for $t \sim 2.10^4$ s, while the local shear rate in the flowing shear band is about 1 s $^{-1}$ in the shear-banding regime and sharply falls down to 0.4 s $^{-1}$ during full fluidization. In the homogeneous flow regime ($t > \tau_f$), $\dot{\gamma}_{eff}$ and both $\dot{\gamma}_{loc}$ collapse to within experimental precision.

Finally, it is worth emphasizing again two important observations drawn from the above analysis. First, as already noted for the stress response $\sigma(t)$ in Fig. 1(a), noticeable fluctuations are reported for slip velocities and local shear rates during transient shear banding whereas the measurements become much smoother once full fluidization is achieved. This points to heterogeneous spatiotemporal dynamics and a two-dimensional view of the local flow field would certainly help to clarify the origin of these fluctuations. Second, our results highlight the importance of very long start-up experiments to ensure that a steady state is reached, especially close to the yield stress, i.e. at small imposed shear rates. Indeed, if the experiment shown above had been stopped after 100 s,

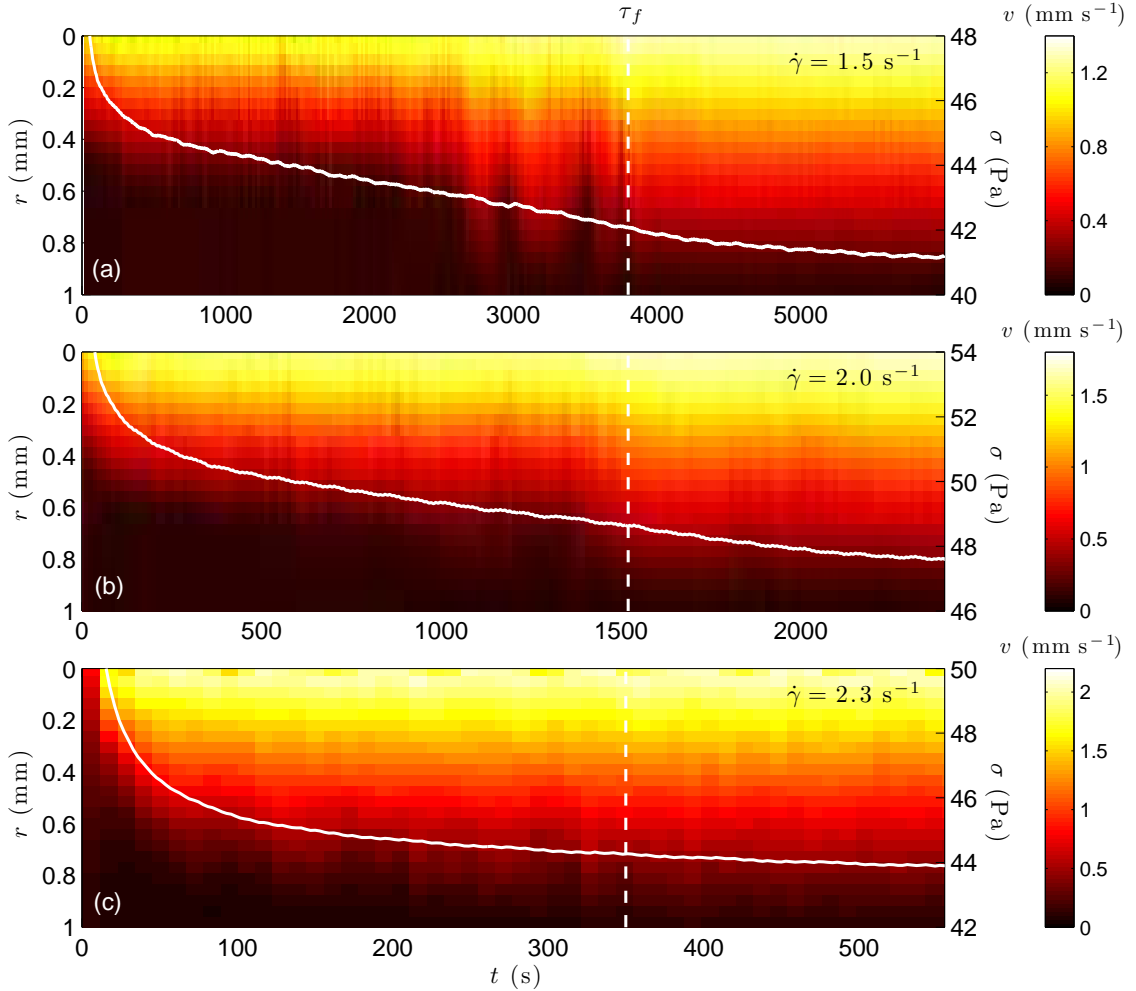


FIG. 7: Spatiotemporal diagrams of the velocity data $v(r, t)$ for an applied shear rate of (a) $\dot{\gamma} = 1.5 \text{ s}^{-1}$, (b) $\dot{\gamma} = 2.0 \text{ s}^{-1}$, and (c) $\dot{\gamma} = 2.3 \text{ s}^{-1}$. White lines are the corresponding stress responses $\sigma(t)$ (right vertical axis). The vertical dashed lines indicate the fluidization times τ_f . The time interval between two velocity profiles is 17 s, 13 s, and 11 s in (a), (b), and (c) respectively. Experiments performed in a smooth Couette cell of gap width 1 mm.

1000 s, or even 10^4 s, one could have mistaken the shear-banded state for the steady state and wrongly categorized our carbopol microgel as a “thixotropic” yield stress fluid. On the contrary, in the present case, a total duration of more than 4.10^4 s allows one to reach the true steady state, namely the homogeneous flow characteristic of a simple yield stress fluid.

D. Influence of the shear rate

To test the robustness of the fluidization scenario described in the previous sections, the imposed shear rate $\dot{\gamma}$ was systematically varied from 0.35 to 10 s^{-1} . In all cases, transient shear banding was observed and the fluidization time was found to decrease sharply with $\dot{\gamma}$. Figure 6 gathers some measurements of the width $\delta(t)$ of the shear band as a function of time. It is clear that the fluidization proceeds faster as $\dot{\gamma}$ is increased. Moreover, for

small shear rates, typically $\dot{\gamma} \lesssim 1 \text{ s}^{-1}$, the shear band remains almost stationary so that the transient shear banding resembles an “induction” period after which the fluidization process dramatically accelerates. For intermediate shear rates, $1 \lesssim \dot{\gamma} \lesssim 2 \text{ s}^{-1}$, the non-zero initial slope of $\delta(t)$ indicates that the shear band slowly grows during the transient shear-banding regime. At $\dot{\gamma} = 2 \text{ s}^{-1}$, a logarithmic growth is observed for $t < 10^3$ s (see red dashed line in Fig. 6), before a sudden acceleration occurs similar to that reported at lower shear rates.

Yet, for $\dot{\gamma} > 2 \text{ s}^{-1}$, there is no such a sharp change that separates the shear-banding regime from the homogeneous flow regime: the shear band rather grows continuously across the gap of the Couette cell. Moreover, between $\dot{\gamma} = 2 \text{ s}^{-1}$ and $\dot{\gamma} = 2.3 \text{ s}^{-1}$, there seems to be a very large drop in the fluidization time for an increase in the applied shear rate of only 15 %. Therefore, we believe that the fluidization scenario goes from an induction-like process followed by an abrupt acceleration

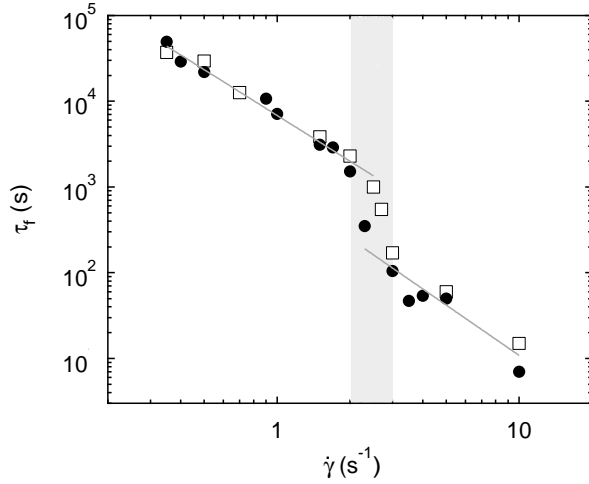


FIG. 8: Fluidization time τ_f as a function of the applied shear rate $\dot{\gamma}$ for two different batches of 1 % w/w carbopol microgels. The grey solid lines are the best power-law fits $\tau_f = A/\dot{\gamma}^\alpha$ of the data for $\dot{\gamma} \leq 2 \text{ s}^{-1}$ ($A = 7.0 \cdot 10^3 \text{ s}^{1-\alpha}$ and $\alpha = 1.8 \pm 0.1$) and for $\dot{\gamma} \geq 3 \text{ s}^{-1}$ ($A = 960 \text{ s}^{1-\alpha}$ and $\alpha = 1.9 \pm 0.3$). The shaded area indicates $\dot{\gamma}^* \simeq 2.5 \pm 0.5 \text{ s}^{-1}$ that separates a transient shear-banding regime characterized by an induction period followed by strong fluctuations from a fast and smooth shear-banding regime where the shear band grows continuously (see text). Filled symbols correspond to the carbopol batch investigated so far in Fig. 1 and Figs. 4–7. Experiments performed in a smooth Couette cell of gap width 1 mm.

with large fluctuations at low $\dot{\gamma}$ to a much smoother and faster process with no induction time at high $\dot{\gamma}$.

Figure 7 further illustrates this change of behaviour by comparing the spatiotemporal diagrams of $v(x, t)$ measured at $\dot{\gamma} = 1.5 \text{ s}^{-1}$, $\dot{\gamma} = 2 \text{ s}^{-1}$, and $\dot{\gamma} = 2.3 \text{ s}^{-1}$ (see also the movies in the supplementary material†). The horizontal scale was chosen so that the fluidization times, respectively 3800 s, 1520 s, and 350 s, graphically coincide. Although the temporal resolution is not as good as for $\dot{\gamma} = 1.5 \text{ s}^{-1}$ due to the smaller time scale, the shear band cannot be seen to take any quasi-stationary position for $\dot{\gamma} = 2.3 \text{ s}^{-1}$ as is the case for $t \lesssim 2500$ s at $\dot{\gamma} = 1.5 \text{ s}^{-1}$. Fluctuations for $t \lesssim \tau_f$ also seem to be absent for the larger shear rate. Finally, the stress signal for $\dot{\gamma} = 2.3 \text{ s}^{-1}$ does not show any sign of kink whereas $\sigma(t)$ does display a small but detectable inflection point around τ_f for $\dot{\gamma} = 1.5 \text{ s}^{-1}$. The experiment at $\dot{\gamma} = 2 \text{ s}^{-1}$ appears as an intermediate case where fluctuations close to τ_f become negligible and the kink in $\sigma(t)$ is hardly visible yet the shear band grows very slowly around $\delta \simeq 0.6 \text{ mm}$ and suddenly accelerates around τ_f . To us, these observations imply that the nature of the transient shear-banding regime changes between the two shear rates shown in Fig. 7(a) and (c), i.e. for a characteristic shear rate $\dot{\gamma}^* \simeq 2.0\text{--}2.3 \text{ s}^{-1}$.

The evolution of τ_f as a function of $\dot{\gamma}$ is shown in Fig. 8. The measurements performed on the batch investigated so far are plotted in filled circles together with another

data set obtained on a different batch in the same smooth Couette geometry (open squares). In this case, reproducibility is very good except maybe at the change of shear-banding regime around $\dot{\gamma}^*$ (see shaded area). In Ref. [15], we reported that the fluidization time decreases as a power-law of $\dot{\gamma}$. In the present data, however, the change of banding regime at $\dot{\gamma}^*$ shows up as a step down in τ_f . Still, the fluidization time behaves as a power law if one considers $\dot{\gamma} < \dot{\gamma}^*$ and $\dot{\gamma} > \dot{\gamma}^*$ separately. Moreover, the best fits yield similar exponents of 1.8 and 2.0 for the two regimes so that the change in shear-banding only appears as a change in the prefactor. We shall further discuss this power-law dependence in Section IV.

E. Influence of the gap width

In this section, we investigate the effect of the gap width by focusing on experiments performed in smooth Couette cells of gap $e = 0.45, 1.5$, and 3 mm . In all cases, a transient shear-banding scenario similar to that described above was found and a fluidization time τ_f can be defined as explained in Sect. III C. As an example, Fig. 9 shows the spatiotemporal diagrams of $v(x, t)$ recorded in the three different Couette cells for similar shear rates $\dot{\gamma} \simeq 0.8 \text{ s}^{-1}$ together with the corresponding stress responses. Transient shear banding is observed for $t < \tau_f$ as indicated by white dotted lines (see also the movies in the supplementary material†). The results for $e = 0.45 \text{ mm}$ are qualitatively similar to those found previously for $e = 1 \text{ mm}$ and $\dot{\gamma} < \dot{\gamma}^*$ [see e.g. $\dot{\gamma} = 1.5 \text{ s}^{-1}$ in Fig. 7(a)], i.e. the transient regime presents a quasi-stationary phase followed by strong fluctuations and abrupt full fluidization. Here, it is interesting to note that the quasi-stationary phase ($t \lesssim 10^3 \text{ s}$) involves a pluglike flow at about half the rotor velocity whose velocity slowly decreases and that precedes the nucleation of a fluctuating shear band (see also the movie in the supplementary material†). This initial plug flow is only seen in smooth geometries and was already evidenced in a previous study devoted to the stress overshoot phenomenon at short times [16].

On the other hand, the spatiotemporal diagrams for $e = 1.5 \text{ mm}$ and $e = 3 \text{ mm}$ resemble that of Fig. 7(c). Indeed, as the gap width is increased, the characteristic kink in $\sigma(t)$ disappears as well as the fluctuations of the flow field, and the shear banding regime becomes more progressive and continuous. Therefore, there exists a clear dependence of the transient shear-banding regime on the gap width and increasing the gap width at a given applied shear rate has the same qualitative effect as increasing the shear rate for a given gap width.

By varying the shear rate for the different gap widths, we observed that the characteristic shear rate $\dot{\gamma}^*$ that separates quasi-stationary then intermittent banding from smooth and continuous banding decreases with e : we found $\dot{\gamma}^* \simeq 4, 0.8$, and 0.5 s^{-1} for $e = 0.45, 1.5$, and 3 mm respectively. This is also reflected in the measurements

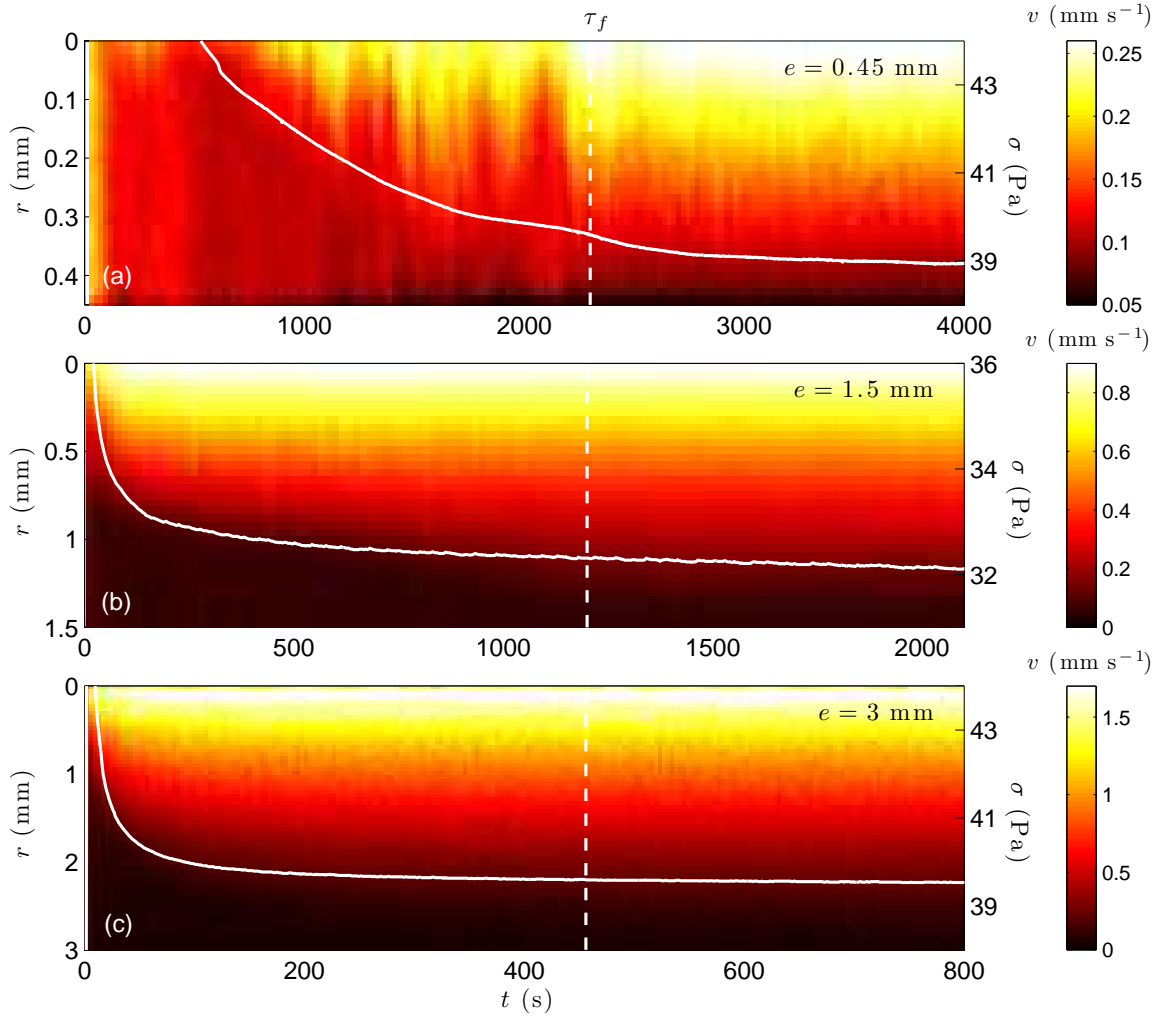


FIG. 9: Spatiotemporal diagrams of the velocity data $v(r, t)$ in smooth Couette cells of different gap widths e and under similar shear rates. (a) $e = 0.45 \text{ mm}$ and $\dot{\gamma} = 0.85 \text{ s}^{-1}$. (b) $e = 1.5 \text{ mm}$ and $\dot{\gamma} = 0.8 \text{ s}^{-1}$. (c) $e = 3 \text{ mm}$ and $\dot{\gamma} = 0.7 \text{ s}^{-1}$. White lines are the corresponding stress responses $\sigma(t)$ (right vertical axis). The vertical dashed lines indicate the fluidization times τ_f . The time interval between two velocity profiles is 21 s, 17 s, and 4 s in (a), (b), and (c) respectively.

of $\delta(t)$ shown in Fig. 10. While the shear-banding regime is characterized by large fluctuations of $\delta(t)$ over almost the whole range of investigated shear rates for the smallest gap width [see Fig. 10(a)], shear banding proceeds in a smooth, continuous manner for most of the shear rates under study at the largest gap width [see Fig. 10(c)]. We also emphasize that the evolution of $\delta(t)$ close to or above $\dot{\gamma}^*$ is generally well fitted by a logarithmic growth (see red dashed lines in Fig. 10).

Finally, the fluidization times are shown in Fig. 11. The characteristic shear rates $\dot{\gamma}^*$ discussed above are indicated as dashed lines. For the lowest shear rate investigated at $e = 3 \text{ mm}$ ($\dot{\gamma} = 0.5 \text{ s}^{-1}$), quasi-stationary banding was observed but the experiment duration was not enough to allow for a measurement of τ_f . Therefore, the corresponding point is not reported in Fig. 11(c) but this experiment still allowed for an estimate of $\dot{\gamma}^*$. Surprisingly, for $e = 0.45 \text{ mm}$ and $e = 1.5 \text{ mm}$, a drop in

τ_f around $\dot{\gamma}^*$ is not as clear as in Fig. 8 for $e = 1 \text{ mm}$. This may be due to a lack of data for $\dot{\gamma} \simeq \dot{\gamma}^*$ but also to a complex dependence of the drop in τ_f on the gap width or on the boundary conditions (see also Sect. IV B below). Following Ref. [15], we chose to fit the τ_f data of Fig. 11 by a single power law over the whole range of investigated shear rates. We find that the power-law behaviour always provide a good description of τ_f vs $\dot{\gamma}$ with an exponent that may depend on the carbopol batch as already noted in Refs. [15, 17].

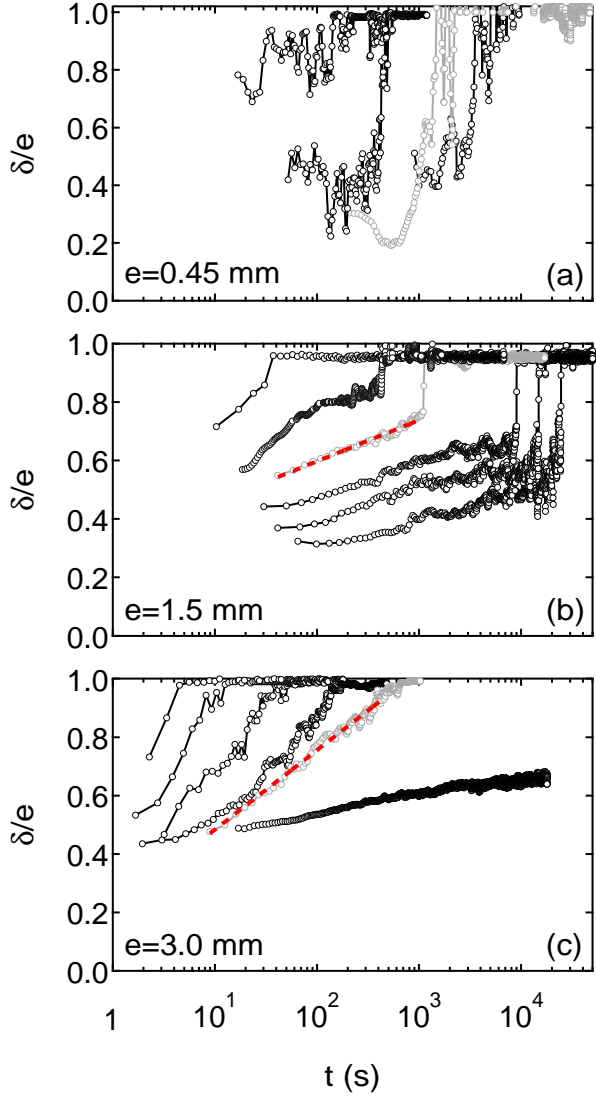


FIG. 10: Width δ of the shear band normalized by the gap width e versus time for different gap widths e and applied shear rates $\dot{\gamma}$. (a) $e = 0.45$ mm and $\dot{\gamma} = 0.6, 0.85, 1.5$, and 3 s^{-1} from right to left. (b) $e = 1.5$ mm and $\dot{\gamma} = 0.4, 0.5, 0.65, 0.8, 1.5$, and 2 s^{-1} from right to left. (c) $e = 3$ mm and $\dot{\gamma} = 0.5, 0.7, 1.2, 2, 3$, and 4.5 s^{-1} from right to left. Gray lines correspond to the shear rates shown in Fig. 9 and red dashed lines are logarithmic fits of $\delta(t)$. Experiments performed in smooth Couette cells on different batches of 1 % w/w carbopol microgels.

IV. DISCUSSION AND OUTLOOK

A. Towards a “phase diagram” for transient shear banding

From Figs. 7 and Fig. 9, one concludes that the gap width and the shear rate are two parameters that control the way transient shear banding proceeds. This leads us to summarize all our data in a single “phase diagram” in the $(e, \dot{\gamma})$ plane as shown in Fig. 12. A rough estimate

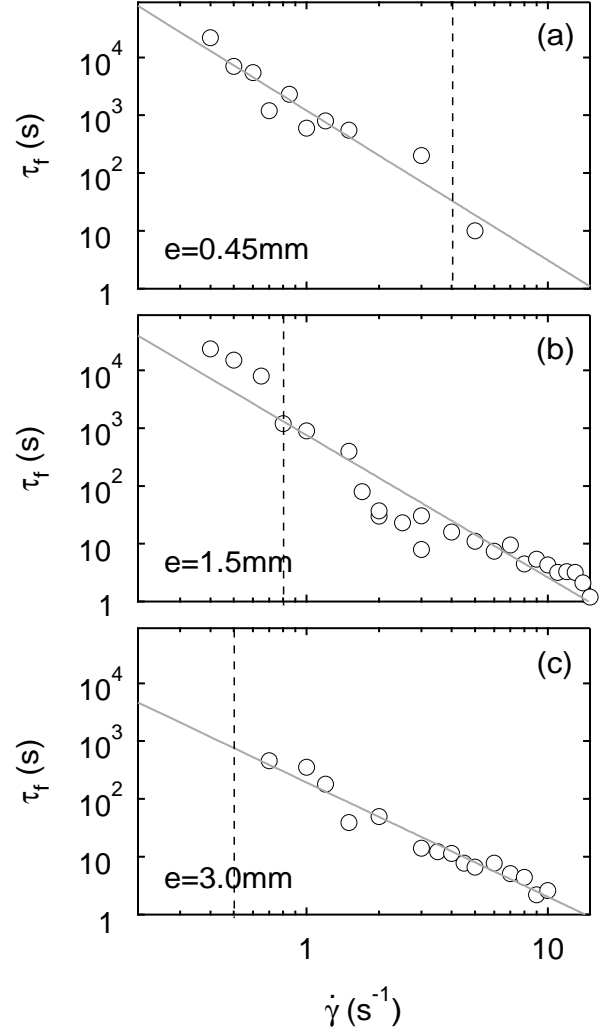


FIG. 11: Fluidization time τ_f as a function of the applied shear rate $\dot{\gamma}$ for various gap widths. The solid lines are the best power-law fits of the data $\tau_f = A/\dot{\gamma}^\alpha$. (a) $e = 0.45$ mm: $A = 1210$ and $\alpha = 2.6 \pm 0.2$. (b) $e = 1.5$ mm: $A = 759$ and $\alpha = 2.4 \pm 0.2$. (c) $e = 3$ mm: $A = 192$ and $\alpha = 2.0 \pm 0.1$. The vertical dashed line indicates $\dot{\gamma}^*$ (see text). Experiments performed in smooth Couette cells on different batches of 1 % w/w carbopol microgels.

for the boundary between the two different shear-banding regimes is $\dot{\gamma}^* \sim 1/e$ (see dashed line).

A possible interpretation of the effect of the gap width lies in the stress heterogeneity inherent to the Couette geometry. Indeed, between the two concentric cylinders, the stress decreases as $1/(R_1 + r)^2$, where R_1 is the rotor radius. In other words, the ratio of the stress σ_1 at the rotor to the stress σ_2 at the stator is $\sigma_1/\sigma_2 = (R_2/R_1)^2$, where R_2 is the stator radius. When the gap width is increased from 0.45 mm to 3 mm, the stress heterogeneity increases from 4 % to about 25 %. Therefore one could conclude that this stress heterogeneity somehow promotes the smooth and continuous transient shear banding regime. However, our observations could also be

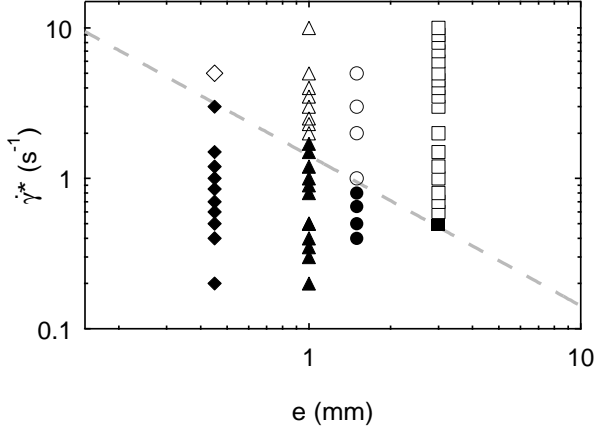


FIG. 12: Type of transient shear-banding regime as a function of the gap width e and the applied shear rate $\dot{\gamma}$. Filled symbols indicate a transient shear banding characterized by an induction period followed by strong fluctuations. Open symbols correspond to a fast and smooth shear-banding regime. The dashed line is $\dot{\gamma}^* \sim 1/e$. Experiments performed in smooth Couette geometries for different batches of 1 % w/w carbopol microgels.

due to confinement rather than to stress heterogeneity. At this stage, more experiments are required to discriminate between the effect of confinement and that of the curved geometry.

B. Influence of boundary conditions

The possible influence of boundary conditions, i.e. surface roughness and physico-chemistry of the cell walls, is another important issue to be explored. In our previous works, [15, 17] we have shown that using sand paper instead of polished Plexiglas as shearing surfaces does not affect the existence of transient shear banding. Except for early stages immediately following the stress overshoot, [17] the shear band develops in the same manner for both boundary conditions. As long as the same carbopol batches are considered, the fluidization times obtained with different boundary conditions are even quantitatively close to each other as shown in Fig. 4 of Ref. [15].

The data for rough boundary conditions was replotted in Fig. 13 together with the fluidization times obtained on a different carbopol batch under mixed boundary conditions (rough rotor, smooth stator, $e = 1.6$ mm, see Sect. II B). Once again, the power-law behaviour of τ_f vs $\dot{\gamma}$ appears as very robust. For the experiments performed in the rough Couette cell of gap 1.1 mm, we estimated $\dot{\gamma}^* \simeq 2 \text{ s}^{-1}$, close to the case of a smooth Couette cell of gap 1 mm (see Sect. III D), while one gets $\dot{\gamma}^* \simeq 3 \text{ s}^{-1}$ for mixed boundary conditions and $e = 1.6$ mm, significantly above the value found for the smooth geometry of gap $e = 1.5$ mm. Yet, in both cases, the fluidization times do not display any sharp break at $\dot{\gamma}^*$ as already

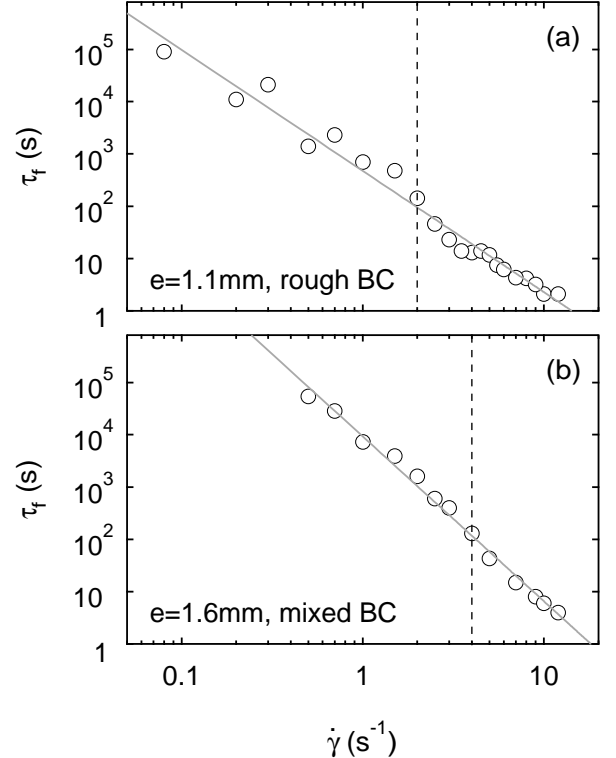


FIG. 13: Fluidization time τ_f as a function of the applied shear rate $\dot{\gamma}$ for various boundary conditions. The solid lines are the best power-law fits of the data $\tau_f = A/\dot{\gamma}^\alpha$. (a) Rough Couette cell of gap $e = 1.1$ mm: $A = 472$ and $\alpha = 2.3 \pm 0.1$. (b) Couette cell of gap $e = 1.6$ mm with a rough rotor and a smooth stator: $A = 9228$ and $\alpha = 3.1 \pm 0.1$. The vertical dashed line indicates $\dot{\gamma}^*$. Experiments performed on different batches of 1 % w/w carbopol microgels.

seen above for $e = 1.5$ mm.

Therefore, although it is clear that the most salient features of transient shear banding are not affected by boundary conditions, subtle effects on $\dot{\gamma}^*$ may be induced by surface effects. Further investigations using systematically the same carbopol batch are still required to settle this open issue.

Finally, it should also be emphasized that the amount of wall slip in steady state for smooth geometries depends on the gap width. We computed the total slip velocity v_s as the sum of slip velocities at the rotor and at the stator recorded once steady state is reached and averaged over at least 150 s. Figure 14 shows v_s relative to the rotor velocity v_0 for various gap widths and applied shear rates. v_s/v_0 is much larger for small gap widths than for larger gaps. For $e = 0.45$ mm, the amount of wall slip is about 30 %, independent of or weakly decreasing with $\dot{\gamma}$. The same trend is observed for $e = 1.5$ mm yet wall slip is smaller and of the order of 15 %. For $e = 3$ mm however, the relative slip sharply decreases with $\dot{\gamma}$ from about 20 % at the lowest shear rate down to negligible values of the order of our uncertainty of about 2 %.

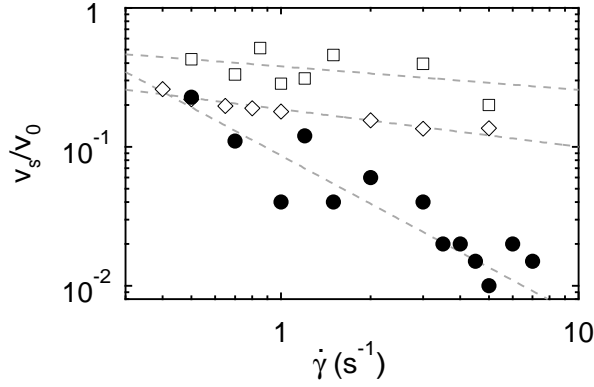


FIG. 14: Steady-state total slip velocity v_s relative to the rotor velocity v_0 as a function of the applied shear rate $\dot{\gamma}$ for smooth Couette geometries of gap width $e = 0.45$ mm (\square), $e = 1.5$ mm (\diamond), and $e = 3$ mm (\bullet). Dotted lines are power laws drawn to guide the eye. Experiments performed on different batches of 1 % w/w carbopol microgels.

C. Local vs global rheology

One last interesting issue concerns the link between steady-state velocity profiles and global rheological data. It is well known that combining standard rheology and velocimetry allows for an analysis of the local rheology [11, 29], i.e. for plotting the *local flow curve* $\sigma(r)$ vs $\dot{\gamma}(r)$. In the Couette geometry, the local stress reads:

$$\sigma(r) = \sigma_1 \left(\frac{R_1}{R_1 + r} \right)^2, \quad (2)$$

the stress at the rotor σ_1 being given by:

$$\sigma_1 = \frac{\Gamma}{2\pi h R_1^2}, \quad (3)$$

where Γ is the torque exerted on the rotor and h is the height of the cell. On the other hand, the local shear rate can be directly extracted from the velocity profiles through:

$$\dot{\gamma}(r) = -(R_1 + r) \frac{\partial}{\partial r} \left(\frac{v(r)}{R_1 + r} \right). \quad (4)$$

The local flow curve can then be compared to the global flow behaviour. Recently, such an analysis has been used to address the link between local and global behaviours in various systems ranging from emulsions [11, 30–32] and granular pastes [29] to industrial materials [33].

In the case of a simple yield stress fluid and in the absence of strong confinement, it is expected that the local and global data collapse [32]. Still, since a complex transient behaviour is involved in our carbopol microgels, it is important to check whether or not the steady state is consistent with such a collapse. In the following, we focus on the data collected in the smooth Couette geometry of gap width $e = 3$ mm since it presents the largest

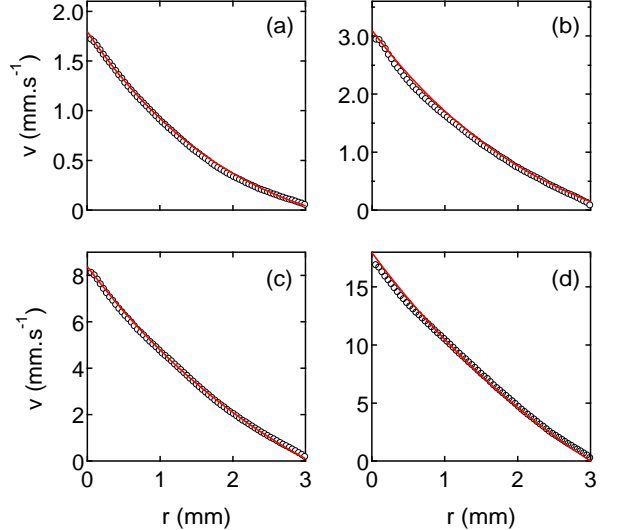


FIG. 15: Velocity profiles $\langle v(r) \rangle$ averaged over a time window of 150 to 600 s in the homogeneous steady-state regime for (a) $\dot{\gamma} = 0.7$ s $^{-1}$, (b) $\dot{\gamma} = 1.2$ s $^{-1}$, (c) $\dot{\gamma} = 3.0$ s $^{-1}$, and (d) $\dot{\gamma} = 6.0$ s $^{-1}$. The red solid lines are the velocity profiles predicted using the Herschel-Bulkley behaviour derived from the global rheological data of Fig. 16. The upper limit of the vertical scale corresponds to the rotor velocity v_0 . Experiments performed in a smooth Couette cell of gap width 3 mm.

stress heterogeneity, i.e. the largest range of local shear rates and stresses for a given applied shear rate. A more thorough investigation of the influence of confinement on the steady-state rheology of carbopol microgels is left for future work.

Figure 15 gathers a few steady-state velocity profiles for $e = 3$ mm obtained by averaging over 100 to 500 individual velocity profiles in the homogeneous regime for $t \gg \tau_f$. Depending on the shear rate, this average corresponds to a time span of 150 to 600 s. The curvature of the velocity profiles is clearly visible for the lowest shear rates: this is both due to the rather large stress variation of about 25 % from the rotor to the stator and to the proximity of the yield stress. As the shear rate is increased and the shear stress departs from the yield stress, velocity profiles become closer to linear.

The local shear rate $\dot{\gamma}(r)$ is easily extracted from steady-state velocity profiles using Eq. (4). On the other hand, we recall that, in the Couette geometry, the global shear stress and shear rate indicated by the rheometer, also referred to as “engineering” data in the literature, are computed respectively from the torque Γ on the inner cylinder and from the angular speed Ω of the rotor according to:

$$\sigma = \frac{R_1^2 + R_2^2}{4\pi h R_1^2 R_2^2} \Gamma. \quad (5)$$

$$\dot{\gamma} = \frac{R_1^2 + R_2^2}{R_2^2 - R_1^2} \Omega, \quad (6)$$

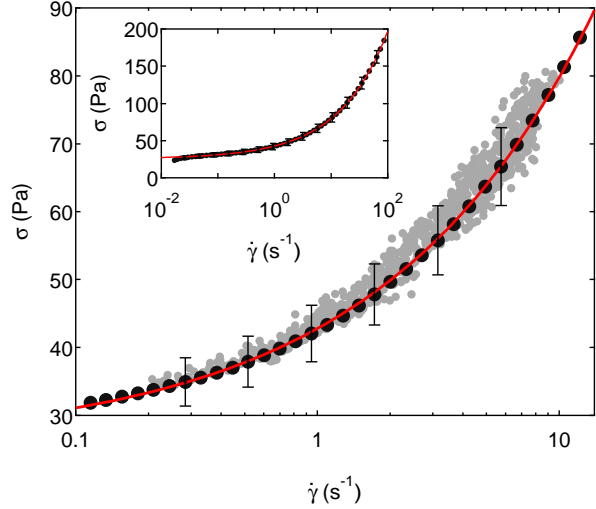


FIG. 16: Local rheology $\sigma(r)$ vs $\dot{\gamma}(r)$ (gray dots) extracted from the steady-state velocity profiles of Fig. 15 (see text) and compared to the global rheological data σ vs $\dot{\gamma}$ (•). The global flow curve was obtained by averaging two independent decreasing shear rate ramps (from 100 s^{-1} down to $1.7 10^{-2} \text{ s}^{-1}$) with a waiting time of 20 s per point and measured respectively before and after the series of start-up experiments under given applied shear rates. The error bars show the difference between the two flow curve measurements. The red line shows the best Herschel-Bulkley fit of the global flow curve for $\dot{\gamma} > 3.5 10^{-2} \text{ s}^{-1}$: $\sigma = \sigma_c + \tilde{\eta} \dot{\gamma}^n$, where $\sigma_c = 25.7 \text{ Pa}$, $n = 0.50$, and $\tilde{\eta} = 17.1 \text{ Pa s}^n$. Inset: full set of global rheological data. Experiments performed in a smooth Couette cell of gap width 3 mm.

Combining Eqs. (3) and (5), one gets

$$\sigma_1 = \frac{2R_2^2}{R_1^2 + R_2^2} \sigma, \quad (7)$$

so that σ_1 is directly deduced from the stress signal $\sigma(t)$ recorded by the rheometer and averaged over the same time window as that used for the velocity profile. The local shear stress $\sigma(r)$ is then computed from Eq. (2). For each applied shear rate, the $\sigma(r)$ vs $\dot{\gamma}(r)$ data are reported in Fig. 16. The dispersion in this local flow curve mainly arises from the experimental estimation of the derivative in Eq. (4) which is based on a simple first-order approximation.

The local flow curve is also compared to the global rheological data in Fig. 16. In order to check that variations in the global flow behaviour remain small in spite of the very long durations of the start-up experiments, we first measured a flow curve σ vs $\dot{\gamma}$ before starting the series of start-up experiments. Once start-up experiments were completed, another flow curve was recorded using the same protocol, namely a decreasing ramp of applied shear rate (from 100 s^{-1} down to $1.7 10^{-2} \text{ s}^{-1}$) with a waiting time of 20 s per point. The data shown in Fig. 16 corresponds to the average of these two flow curves and the error bars indicate their difference. This difference reflects a global shift of the flow curve by a few

pascals, which we attribute to a slow drift of the material properties due to repeated shearing protocols over more than 10^4 s. The average flow curve is perfectly fit by a Herschel-Bulkley behaviour, $\sigma = \sigma_c + \tilde{\eta} \dot{\gamma}^n$, for shear rates larger than $3.5 10^{-2} \text{ s}^{-1}$. At low shear rates, the deviation from Herschel-Bulkley behaviour (see inset of Fig. 16) is attributed to paramount wall slip effects as already reported in the literature [34, 35].

The agreement between local and global rheology shown in Fig. 16 is quite remarkable. It can be further confirmed by computing the velocity profiles based on the Herschel-Bulkley behaviour inferred from the global rheological measurements and transferred locally:

$$\sigma(r) = \sigma_c + \tilde{\eta} \dot{\gamma}(r)^n \text{ for } \sigma(r) \geq \sigma_c. \quad (8)$$

Indeed, inserting Eq. (8) into Eq. (4) and integrating over r yields:

$$\frac{v(r)}{R_1 + r} = \frac{v_1}{R_1} - \int_0^r \frac{dx}{R_1 + x} \left[\frac{\sigma_1 \left(\frac{R_1}{R_1 + x} \right)^2 - \sigma_c}{\tilde{\eta}} \right]^{1/n}, \quad (9)$$

where v_1 stands for the velocity of the fluid at the rotor, i.e. $v_1 = v(0)$. In practice, v_1 is estimated by a linear extrapolation of the time-averaged velocity profile at $r = 0$ and σ_1 is obtained from the rheometer measurement as explained above. Therefore, once the Herschel-Bulkley parameters σ_c , $\tilde{\eta}$, and n are known from independent global measurements, the velocity profile can be predicted from Eq. (9) without any free parameter. The results of the computations based on Eq. (9) are superimposed to the experimental velocity profiles as solid lines in Fig. 15. Once again, the agreement is excellent, which shows that a single Herschel-Bulkley law allows to predict all the velocity profiles quite well. This confirms that our carbopol microgel behaves as expected for simple yield stress fluids in steady state, at least when confinement effects are negligible [31, 32].

V. SUMMARY AND CONCLUSION

In this paper, we have reported an extensive study of the transient shear-banding phenomenon observed in carbopol microgels in very long start-up experiments under controlled shear rate. By varying both the shear rate $\dot{\gamma}$ and the gap width e in the concentric cylinder geometry, this data set completes our previous study [15] and sheds new light on the fluidization dynamics of a simple yield stress fluid.

In particular, for low applied shear rates (typically smaller than 1 s^{-1}) or for small gap widths (typically smaller than 1 mm), the fluidization process involves the nucleation of shear band that remains almost stationary for several hours before large fluctuations give way to a homogeneous flow. This rather abrupt fluidization shows up on the stress response as a kink separating a

quasi-stationary but fluctuating phase from full relaxation, which is also seen in the cone-and-plate geometry. For larger applied shear rates or for larger gap widths, the transient shear band is seen to continuously grow and invade the whole sample. In this case, no clear rheological signature can be associated with the fluidization process. The growth of the shear band is close to logarithmic in time, which is reminiscent of structural aging phenomena in granular matter and in gelatin gels under stress [36–38].

Moreover, the fluidization time τ_f , defined as the time after which the flow is homogeneously sheared, decreases as a power-law of the applied shear rate $\dot{\gamma}$, $\tau_f \sim \dot{\gamma}^{-\alpha}$ with an exponent $\alpha = 1.8$ to 3.1 , which mostly depends on the carbopol batch. In most cases, τ_f vs $\dot{\gamma}$ does not show any clear sign of the transition between the two above regimes for transient shear banding, although more experiments are still needed to draw definite conclusions on the “phase diagram” in the $(e, \dot{\gamma})$ plane proposed in Sect. IV A. Finally, we have shown that boundary conditions seem to have a negligible influence on the long-time fluidization process and we checked that once a true steady state is reached, i.e. once transient shear banding has led to homogeneous flow, the local flow curve inferred from velocity profiles nicely collapses onto global rheological data, which follow a Herschel-Bulkley behaviour.

The question remains whether the transient shear banding phenomenon explored here in carbopol micro-gels is shared by other simple yield stress fluids such as foams and emulsions. To provide an answer, future research should concentrate on revisiting previous studies

with emphasis on small shear rates and on long start-up experiments. Indeed, transient shear banding regimes may have been missed in previous studies due to the use of too large shear rates and/or too large gap widths. In other cases, it may have also been wrongly interpreted in terms of stationary shear banding due to too short recording durations. The present study suggests that similar experiments should be conducted systematically on foams and emulsions following a rigorous rheological protocol so that the results obtained on different systems can be easily compared. Besides a possible universality in the fluidization processes of simple yield stress fluids, our results also raise the issue of the structure of the transient shear band: what are the microstructural differences, if any, between the fluidized and the solidlike material? To answer this question, experiments coupling time-resolved local visualization, e.g. through confocal microscopy, and rheometry are required on samples that allow for a fine tuning of the microstructural features, such as the size of jammed particles, their degree of softness, and their interactions.

Acknowledgments

We thank Y. Forterre for providing us with the carbopol, V. Grenard for substantial help with the software, and H. Feret for technical help. We also thank L. Bocquet, A. Colin, and G. Ovarlez for several enlightening discussions.

-
- [1] H. A. Barnes, *J. Non-Newtonian Fluid Mech.*, 1999, **81**, 133–178.
 - [2] E. R. Weeks, Statistical Physics of Complex Fluids, 2007, pp. 243–255.
 - [3] P. Coussot, *Soft Matter*, 2007, **3**, 528–540.
 - [4] P. C. F. Møller, J. Mewis and D. Bonn, *Soft Matter*, 2006, **2**, 274–283.
 - [5] G. P. Roberts and H. A. Barnes, *Rheol. Acta*, 2001, **40**, 499–503.
 - [6] P. C. F. Møller, A. Fall and D. Bonn, *Europhys. Lett.*, 2009, **87**, 38004.
 - [7] P. Coussot, J. S. Raynaud, F. Bertrand, P. Moucheront, J. P. Guilbaud, H. T. Huynh, S. Jarny and D. Lesueur, *Phys. Rev. Lett.*, 2002, **88**, 218301.
 - [8] P. C. F. Møller, S. Rodts, M. A. J. Michels and D. Bonn, *Phys. Rev. E*, 2008, **77**, 041507.
 - [9] A. Ragouilliaux, G. Ovarlez, N. Shahidzadeh-Bonn, B. Herhaft, T. Palermo and P. Coussot, *Phys. Rev. E*, 2007, **76**, 051408.
 - [10] P. C. F. Møller, A. Fall, V. Chikkadi, D. Derkx and D. Bonn, *Phil. Trans. R. Soc. Lond. A*, 2009, **367**, 5139–5155.
 - [11] J.-B. Salmon, L. Béchu, S. Manneville and A. Colin, *Eur. Phys. J. E*, 2003, **10**, 209–221.
 - [12] R. Höhler and S. C. Addad, *J. Phys.: Condens. Matter*, 2005, **17**, 1041–1069.
 - [13] G. Ovarlez, S. Rodts, X. Chateau and P. Coussot, *Rheol. Acta*, 2009, **48**, 831–844.
 - [14] J. Mewis and N. Wagner, *Adv. Colloid Interface Sci.*, 2009, **147–148**, 214–227.
 - [15] T. Divoux, D. Tamarii, C. Barentin and S. Manneville, *Phys. Rev. Lett.*, 2010, **104**, 208301.
 - [16] T. Divoux, C. Barentin and S. Manneville, *Soft Matter*, 2011, **7**, 9335–9349.
 - [17] T. Divoux, C. Barentin and S. Manneville, *Soft Matter*, 2011, **7**, 8409–8418.
 - [18] L. Baudonnet, J.-L. Grossiord and F. Rodriguez, *J. Dispersion Sci. Technol.*, 2004, **25**, 183–192.
 - [19] R. J. Ketz, R. K. Prud'homme and W. W. Graessley, *Rheol. Acta*, 1988, **27**, 531–539.
 - [20] J.-Y. Kim, J.-Y. Song, E.-J. Lee and S.-K. Park, *Colloid Polym. Sci.*, 2003, **281**, 614–623.
 - [21] F. K. Oppong, L. Rubatat, A. E. Bailey, B. J. Friskin and J. R. de Bruyn, *Phys. Rev. E*, 2006, **73**, 041405.
 - [22] D. Lee, I. A. Gutowski, A. E. Bailey, L. Rubatat, J. R. de Bruyn and B. J. Friskin, *Phys. Rev. E*, 2011, **83**, 031401.
 - [23] J. M. Piau, *J. Non-Newtonian Fluid Mech.*, 2007, **144**, 1–29.
 - [24] P. Coussot, L. Tocquer, C. Lanos and G. Ovarlez, *J.*

- Non-Newtonian Fluid Mech.*, 2009, **158**, 85–90.
- [25] G. Benmouffok-Benbelkacem, F. Caton, C. Baravian and S. Skali-Lami, *Rheol. Acta*, 2010, **49**, 305–314.
 - [26] S. Manneville, L. Béchu and A. Colin, *Eur. Phys. J. AP*, 2004, **28**, 361–373.
 - [27] T. Gibaud, C. Barentin and S. Manneville, *Phys. Rev. Lett.*, 2008, **101**, 258302.
 - [28] T. Gibaud, C. Barentin, N. Taberlet and S. Manneville, *Soft Matter*, 2009, **5**, 3026–3037.
 - [29] N. Huang, G. Ovarlez, F. Bertrand, S. Rodts, P. Coussot and D. Bonn, *Phys. Rev. Lett.*, 2005, **94**, 028301.
 - [30] L. Béchu, S. Manneville and A. Colin, *Phys. Rev. Lett.*, 2006, **96**, 138302.
 - [31] J. Goyon, A. Colin, G. Ovarlez, A. Ajdari and L. Bocquet, *Nature*, 2008, **454**, 84–87.
 - [32] G. Ovarlez, S. Rodts, A. Ragouilliaux, P. Coussot, J. Goyon and A. Colin, *Phys. Rev. E*, 2008, **78**, 036307.
 - [33] A. Ragouilliaux, B. Herzhaft, F. Bertrand and P. Coussot, *Rheol. Acta*, 2006, **46**, 261–271.
 - [34] S. P. Meeker, R. T. Bonnecaze and M. Cloitre, *Phys. Rev. Lett.*, 2004, **92**, 198302.
 - [35] S. P. Meeker, R. T. Bonnecaze and M. Cloitre, *J. Rheol.*, 2004, **48**, 1295–1320.
 - [36] L. Bocquet, E. Charlaix, S. Ciliberto and J. Crassous, *Nature*, 1998, **396**, 735–737.
 - [37] H. Gayvallet and J.-C. Géminard, *Eur. Phys. J. B*, 2002, **30**, 369–375.
 - [38] O. Ronsin, C. Carolin and T. Baumberger, *Phys. Rev. Lett.*, 2009, **103**, 138302.